Microstructural evolution and Poisson ratio of epitaxial ScN grown on TiN(001)/MgO(001) by ultrahigh vacuum reactive magnetron sputter deposition

D. Gall, I. Petrov, P. Desjardins, and J. E. Greene[a)]
Materials Science Department, Coordinated Science Laboratory, and Materials Research Laboratory, University of Illinois, 1101 West Springfield Avenue, Urbana, Illinois 61801

(Received 3 May 1999; accepted for publication 17 August 1999)

ScN layers, 60–80 nm thick, were grown at 800 °C on 220-nm-thick epitaxial TiN(001) buffer layers on MgO(001) by ultrahigh vacuum reactive magnetron sputter deposition in pure N_2 discharges. The films are stoichiometric with N/Sc ratios, determined by Rutherford backscattering spectroscopy and x-ray photoelectron spectroscopy, of 1.00 ± 0.02. Plan-view and cross-sectional transmission electron microscopy analyses showed that the films are single crystals which appear defect free up to a critical thickness of $\simeq 15$ nm, above which an array of nanopipes form with their tubular axis along the film growth direction and extending to the free surface. The nanopipes are rectangular in cross section with areas of $\simeq 1.5\times5\ \mathrm{nm}^2$ and are self-organized along $\langle 100\rangle$, directions with an average separation of $\simeq 40$ nm. Their formation is the result of periodic kinetic surface roughening which leads to atomic self-shadowing and, under limited adatom mobility conditions, to deep cusps which are the origin of the nanopipes. The ScN layers are nearly relaxed, as determined from x-ray diffraction θ-2θ scans in both reflection and transmission, with only a small residual compressive strain due to differential thermal contraction. The Poisson ratio of ScN was found to be 0.20 ± 0.04, in good agreement with *ab initio* calculations. © *1999 American Institute of Physics.* [S0021-8979(99)09722-4]

I. INTRODUCTION

Transition-metal (TM) nitrides are well known for their remarkable physical properties including high hardness and mechanical strength, chemical inertness, and electrical resistivities that vary from metallic to semiconducting. As a result, they are widely studied and have become technologically important for applications such as hard wear-resistant coatings, diffusion barriers, and optical coatings. While TiN has received by far the most attention and is presently used commercially in all of the above mentioned applications, the neighboring nitride on the periodic table, ScN, remains almost totally unexplored.

We have recently reported the growth of stoichiometric polycrystalline ScN layers on MgO(001) by ultrahigh vacuum reactive magnetron sputter deposition at 750 °C.[1] The films were strongly textured, both in-plane and along the growth direction, with a columnar microstructure. During nucleation and the early stages of film growth, the layers consisted of approximately equal volume fractions of 002 and 111 oriented grains. However, preferred orientation evolved toward a purely 111 texture within $\simeq 40$ nm as the 002 grains grow out of existence in a kinetically limited competitive growth mode. The temperature dependence of the electrical resistivity indicated semiconducting behavior and optical absorption measurements showed a well defined edge corresponding to a direct transition at 2.37 ± 0.05 eV. Low-energy N_2^+ irradiation during film growth, with an incident N_2^+ to Sc ratio of 14, was used to obtain single crystal ScN layers on MgO(001).[2] Films deposited with N_2^+ energies $E_{N_2^+}\geqslant 20$ eV exhibited a cube-on-cube epitaxial relationship with the substrate. The hardness H and elastic modulus E of epitaxial ScN(001) layers grown with $E_{N_2^+}=20$ eV were 21.1 and 356 GPa, respectively.

In this article, we report results on the growth by reactive magnetron sputter deposition of ScN single crystals on epitaxial TiN(001) buffer layers on MgO(001). The buffer layers slightly reduce the lattice mismatch from 6.1% to 5.7% and, more importantly, prevent Sc from reacting with MgO during the early stages of growth at the deposition temperature, $T_s=800$ °C, used in these experiments. The ScN layers grow relatively defect free up to a thickness of 15 nm. At higher thicknesses, nanopipes are formed along the film growth direction. The rectangular nanopipes, with cross-sectional areas of $\simeq 1.5\times5\ \mathrm{nm}^2$, are self-organized along orthogonal $\langle 100\rangle$ directions. Their formation is the result of kinetic surface roughening giving rise to atomic self-shadowing due to limited adatom mobilities. This, in turn, leads to deep cusps which are the origin of the nanopipes. The Poisson ratio of ScN, 0.20 ± 0.04, was determined from reflection and transmission x-ray diffraction measurements. Calculated values, based on density functional theory and the generalized gradient approximation, are in good agreement.

II. EXPERIMENTAL PROCEDURE

All films were grown in a two-chamber turbomolecular-pumped ultrahigh vacuum (UHV) deposition system consist-

[a)]Electronic mail: greene@mrlxp2.mrl.uiuc.edu

 © 1999 American Institute of Physics

ing of a sample introduction chamber which was evacuated to 5×10^{-8} Torr (6.7×10^{-6} Pa) prior to sample transfer and a three-target magnetron growth chamber with a base pressure of 1×10^{-9} Torr (1.3×10^{-7} Pa). The sputtering targets were 5-cm-diameter water-cooled disks. The Ti target has a purity of 99.999% while the Sc is 99.9% pure with the only contaminant detectable by Rutherford backscattering spectroscopy (RBS) being 0.1 at. % Ta, the normal impurity in Sc. Sputter deposition of both the TiN buffer layers and the ScN overlayers were carried out in pure N_2 (99.999%), introduced through a high precision solenoid valve, at 5 mTorr (0.7 Pa). The pressure was measured by a capacitance nanometer and maintained constant with an automatic mass-flow controller. Current-regulated dc power supplies were used to provide a discharge current of 0.5 A at 485 V for TiN and 1.5 A at 312 V for ScN deposition. The resulting deposition rates, with a target-to-substrate separation of 15 cm, were 132 and 186 nm h^{-1}, respectively, in the fully target-nitrided regime. Each target was sputter etched for 5 min, with shutters shielding the substrate and the other target, immediately prior to initiating deposition.

The substrates were polished $10\times10\times0.5$ mm^3 MgO(001) wafers which were cleaned and degreased by successive rinses in ultrasonic baths of trichloroethane, acetone, methanol, and deionized water and blown dry in dry N_2. They were then mounted on resistively heated Ta platens using a Mo clip and inserted into the sample introduction chamber for transport to the deposition chamber. Final substrate cleaning consisted of thermal degassing at 800 °C for 1 h, a procedure shown to result in sharp MgO(001)1×1 reflection high energy electron diffraction patterns.[3] Film growth temperature, including the contribution due to plasma heating, was measured using a pyrometer calibrated by a thermocouple that was bonded to a dummy MgO wafer. The TiN buffer layer was deposited at 750 °C, the temperature raised to 800 °C, and the ScN overlayer was grown without breaking vacuum. Following deposition, the samples were allowed to cool to <100 °C before transfer to the load lock chamber which was then vented with dry N_2.

Plasma characteristics at the substrate during film growth were determined from probe measurements following procedures described elsewhere.[4] The floating potential V_s and the plasma potential V_p were determined to be -4 and 0 V, respectively, resulting in an incident N_2^+ ion energy during film growth of $E_{N_2^+}=4$eV. The incident N_2^+ to Sc ratio was found to be $J_{N_2^+}/J_{Sc}=1.7$. Both $E_{N_2^+}$ and $J_{N_2^+}/J_{Sc}$ are much less than the values, 20 eV and 14, used in our previous experiments employing magnetically unbalanced magnetron sputter deposition[2] and we expect N_2^+ irradiation in the present case to have relatively little effect on adatom mobilities and surface roughening kinetics.

Film microstructure and texture were investigated using a combination of x-ray diffraction (XRD), plan-view transmission electron microscopy (TEM), and cross-sectional TEM (XTEM). The XRD measurements were carried out in a Rigaku 200 instrument with a Mo $K_{\alpha1}$ ($\lambda=0.070\,930$ nm) rotating anode source operated at 45 kV and 100 mA. Using a monochromatized beam, the apparatus provides a 2θ resolution of 0.01°. ScN films were analyzed in both reflection and transmission. In the standard reflection mode, the incoming beam is diffracted from (002) planes parallel to the substrate surface whereas in transmission, the sample is rotated by 90° such that (200) planes are sampled and the diffracted beam passes through the substrate. The combination of these two measurements provides both the perpendicular $a_\perp$ and parallel $a_\parallel$ lattice constants and thus a direct measure of film strain.

Surface roughness was quantitatively determined by high-resolution x-ray reflectivity. The experiments were performed in a Philips X-Pert MRD system using a Cu $K_{\alpha1}$ beam ($\lambda=0.154\,0597$ nm) monochromatized by passing it through a Ge(220) four-crystal monochromator, yielding a spectral width of 7×10^{-5}. Reflected intensities were collected using a parallel-plate graphite monochromator.

A Philips CM12 microscope with a LaB_6 filament operated at 120 kV was used for the TEM and XTEM analyses. Plan-view specimens were obtained by first mechanically grinding from the back side to a thickness of $\simeq30$ μm. Final thinning to electron transparency was accomplished by ion milling using a 5.5 kV Ar^+-ion beam incident initially at 14° and then decreased to 12°. Cross-sectional specimens were prepared by gluing two samples film-to-film and then cutting vertical sections which were ground and ion milled in a manner similar to that of the plan-view samples, but from both sides.

The microchemistry of as-deposited films was examined using a combination of RBS and x-ray photoelectron spectroscopy (XPS). The RBS probe beam consisted of 2 MeV He^+ ions incident at 22.5° relative to the sample surface normal with the detector set at a 150° scattering angle. XPS measurements were carried out in a Perkin-Elmer PHI 5400 spectrometer equipped with a Mg K_α x-ray source and a hemispherical detector. XPS depth profiles were obtained from both uncapped ScN layers and samples which were capped *in situ* with a 20-nm-thick epitaxial *W* layer grown at 700 °C. The *W* caps, which prevented air exposure during transfer between the deposition and analysis chambers, were removed by 3 keV Ar^+ sputter etching using beam rastering over a 3×3 mm^2 area. Etching was continued until *W* was no longer detected. ScN ion etching rates were obtained from samples of known initial thickness determined from XTEM and x-ray reflectivity measurements.

III. RESULTS AND DISCUSSION

The composition of the ScN layers was measured by RBS and the spectra analyzed using the RUMP simulation program.[5] The results show that the films are stoichiometric with a N/Sc ratio of 1.00 ± 0.02. An additional measure of the film composition was provided by XPS. In this case, the N/Sc ratio was determined by fitting the N 1*s* and Sc 2*p* peaks with asymmetric Gaussian–Lorentzian curves and using sensitivity factors from Ref. 6. The results, N/Sc$=1.00$ ±0.05, are in agreement with the RBS data. No impurities, other than the 0.1 at. % Ta from the Sc target were detected by either RBS or XPS.

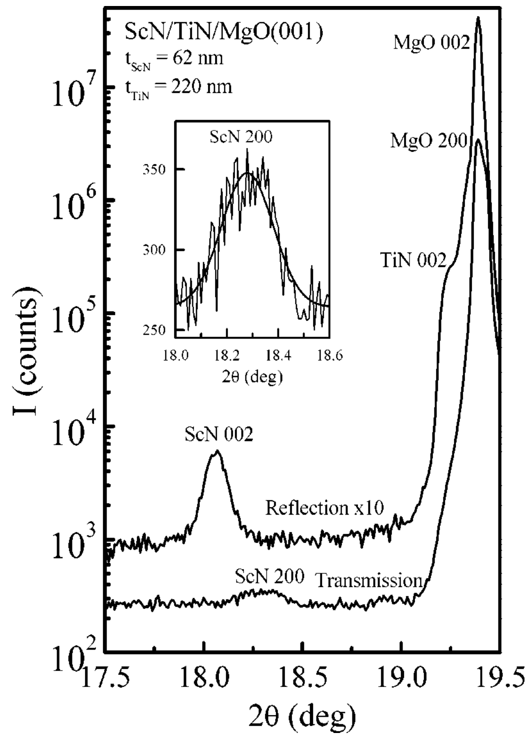

FIG. 1. XRD $\theta-2\theta$ scans in transmission and reflection from an epitaxial 62-nm-thick ScN layer grown on TiN/MgO(001). The inset shows a Gaussian fit of the ScN (200) peak.

Narrow regions of typical XRD reflection and transmission θ-2θ scans are shown in Fig. 1 for a bilayer ScN/TiN/MgO(001) sample in which the layer thicknesses were $t_{\mathrm{TiN}}=220$ nm and $t_{\mathrm{ScN}}=62$ nm. The scans, offset by one decade to avoid overlap, contain only (00*l*) peaks in reflection and (*h*00) peaks in transmission, indicating that both the NaCl-structure ScN overlayer and the TiN buffer layer grow with a cube-on-cube orientational relationship to the substrate: $(001)_{\mathrm{ScN}}\|(001)_{\mathrm{TiN}}\|(001)_{\mathrm{MgO}}$ and $[100]_{\mathrm{ScN}}\|[100]_{\mathrm{TiN}}\|[100]_{\mathrm{MgO}}$. The MgO, TiN, and ScN 002 reflection peaks at $2\theta=19.39°, 19.23°$, and $18.06°$ correspond to lattice constants along the film growth direction $a_{\perp}$ of 0.4213, 0.4247, and 0.4519 ± 0.0005 nm, respectively. The perpendicular MgO lattice constant is in perfect agreement with reference data.[7] However, both $a_{\perp,\mathrm{TiN}}$ and $a_{\perp,\mathrm{ScN}}$ are larger than previously published relaxed values, $a_{\mathrm{TiN}}=0.4242$ nm (Ref. 7) and $a_{\mathrm{ScN}}=0.4501$ nm (see below), indicating that the layers are in a state of mild in-plane compressive stress.

The position of the MgO 200 peak, obtained in transmission (lower scan in Fig. 1 corresponding to diffraction from lattice planes parallel to the growth direction), is identical to that of the MgO 002 peak as expected. However, the TiN 200 peak is shifted to higher angles (lower in-plane lattice constant) due to the in-plane compressive strain and cannot be resolved from the intense MgO substrate peak. The ScN 200 peak position is at $2\theta=18.28°$ yielding an in-plane lattice constant $a_{\|,\mathrm{ScN}}=0.4465\pm0.0005$ nm compared to $a_{\perp,\mathrm{ScN}}=0.4519$nm. The Gaussian fit used to determine the 200 peak position is shown in the inset in Fig. 1. The intensities of the transmission peaks are weaker than those in the reflection scan due to x-ray absorption by the 0.5-mm-thick MgO substrate, while the higher background intensity stems from additional diffuse scattering.

The above results show that the in-plane ScN and TiN lattice constants are smaller than, with the perpendicular values being larger than, the corresponding relaxed lattice constants. Thus, both the buffer layer and the overlayer are in compression. Based upon ScN and TiN elastic constants of 356 GPa[2] and 445 GPa,[8] the stress σ_{ScN} in the ScN layer is 3.6 GPa while σ_{TiN} is estimated as $\simeq 1.8$ GPa. The compressive stress in TiN is completely due, and that of ScN is primarily due, to differential thermal contraction during cooling from the film growth temperature, 800 °C, to room temperature. The thermal expansion coefficients for ScN, TiN, and MgO are 4×10^{-6} K^{-1} (Ref. 9), 9×10^{-6} K^{-1} (Ref. 10), and 1.3×10^{-5} K^{-1} (Ref. 11), respectively. Assuming fully relaxed layers during growth, no relaxation during the cooling process, and using a TiN Poisson ratio of $\nu_{\mathrm{TiN}}=0.22$,[12] yields an expected TiN 2θ 002 peak position of 19.22°, in good agreement with the observed 2θ position at 19.23°.

The measured in-plane ScN lattice constant is 0.8% $\pm0.1\%$ smaller than the relaxed value. This is a slightly larger compressive strain than can be accounted for by differential thermal contraction, $0.70\%\pm0.07\%$. The ScN layer is therefore not completely relaxed at the growth temperature where it retains a residual compressive strain of $\simeq0.1\%$. This, however, is quite small compared to the lattice constant misfit, 6.1%, at 800 °C.

The relaxed lattice constant for ScN was measured using a polycrystalline 180-nm-thick ScN film grown under the same conditions as the single crystal layers but with a SiO_2/Si substrate in which the 0.6-nm-thick SiO_2 layer was obtained by thermal oxidation. XRD $\omega-2\theta$ measurements using asymmetric reflections showed the layer to be essentially stress free. Lattice parameter values determined from 111, 002, and 402 peak positions obtained from θ–2θ XRD scans were in excellent agreement yielding a relaxed lattice parameter of 0.4501 ± 0.0002 nm. This is within the range of previously published ScN lattice constants, 0.4500–0.4505 nm.[9,13–15]

Using the relaxed ScN lattice constant given above, the inplane and orthogonal strains ϵ in the epitaxial layer are $\epsilon_{\|}=0.80\%$ and $\epsilon_{\perp}=-0.40\%$,respectively. The Poisson ratio ν was then calculated from the following relationship:

$$\nu=\frac{\epsilon_{\perp}/\epsilon_{\|}}{(\epsilon_{\perp}/\epsilon_{\|})-2}. \tag{1}$$

We obtain $\nu_{\mathrm{ScN}}=0.20\pm0.04$. This is comparable with known Poisson ratios for other transition-metal nitrides which range from $\nu_{\mathrm{ZrN}}=0.19$ (Ref. 16) to $\nu_{\mathrm{TiN}}=\nu_{\mathrm{NbN}}=0.22$ (Refs. 12 and 17).

As an additional check of our experimentally measured value for the Poisson ratio, we have employed *ab initio* methods, following the procedure in Ref. 18, using the generalized gradient approximation, a plane-wave basis set, and ultrasoft pseudopotentials to calculate the bulk modulus K and ν_{ScN}. We obtain $K=187$ GPa which agrees well with our previously measured value of 182 GPa.[2] Calculation of

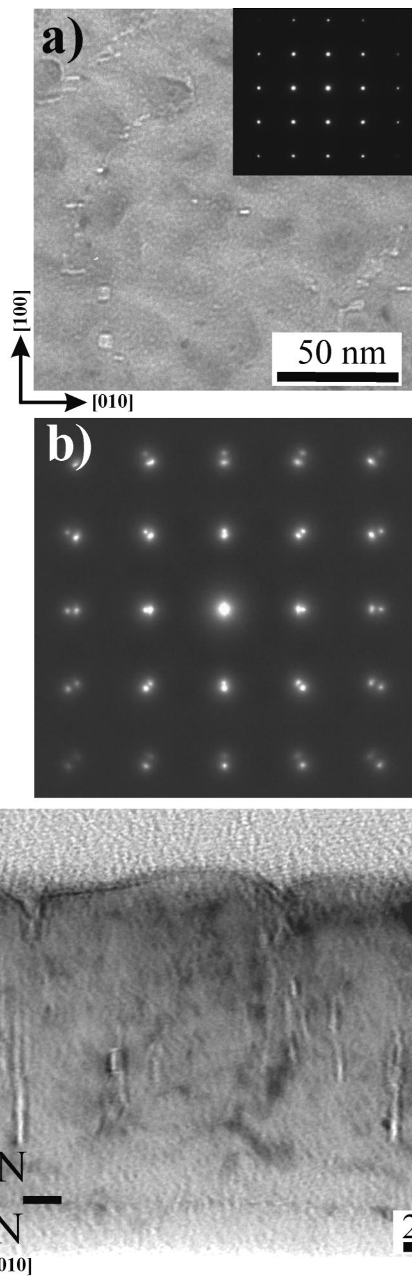

FIG. 2. (a) Bright-field TEM micrograph with a corresponding SAED pattern from an epitaxial ScN film grown on TiN/MgO(001); (b) SAED pattern from the XTEM micrograph in (c) obtained from the same sample.

ν_{ScN} along the $\langle 100 \rangle$ direction yields 0.20 ± 0.01 in agreement with our present experimental results.

Typical plan-view and cross-sectional TEM images with corresponding selected area electron diffraction (SAED) patterns, in this case from an 82-nm-thick ScN film deposited on a TiN(001) buffer layer, are shown in Fig. 2. The 001 [Fig. 2(a)] and 100 [Fig. 2(b)] zone axis diffraction patterns both exhibit symmetric reflections characteristic of single crystals. The 100 XTEM diffraction pattern, obtained with a 0.4-μm aperture centered at the ScN/TiN interface, contains two sets of reflections separated by a distance consistent with the lattice-constant mismatch between ScN and TiN. XTEM tilting experiments reveal an abrupt ScN/TiN interface, with misfit dislocations visible, at the position indicated in Fig. 2(c). All ScN layers appear defect-free (other than the presence of dislocations) up to a thickness t_c of $\simeq 15$ nm. Above the defect-free region, nanopipes with a width of $\simeq 1.5$ nm extend along the growth direction and continue to the free surface where they terminate at cusps. The nanopipes appear as bright squares and rectangles in the plan-view image [Fig. 2(a)]. The apparent termination of some nanopipes below the surface in Fig. 2(c) is due to a gradient in the thickness of the XTEM specimen which is thinnest at the TiN buffer layer and thickest at the ScN free surface. The nanopipes exhibit contrast reversal in under- and overfocus imaging.

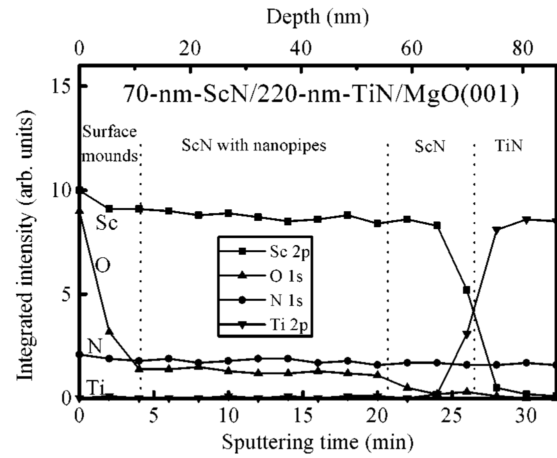

FIG. 3. XPS profiles from a 70-nm-thick epitaxial ScN layer grown on TiN/MgO(001) showing the Sc 2p, O 1s, N 1s, and Ti 2p intensities as a function of sample depth.

XPS depth profile measurements from uncapped samples also provide evidence for the presence of nanopipes. Figure 3 shows a typical depth profile from a 70-nm-thick ScN layer on TiN/MgO(001). The relative intensity of the Sc 2p, N 1s, O 1s, and Ti 2p peaks are plotted versus sample depth. The near-surface oxygen concentration is high due to sample air exposure, atomic mixing during ion etching, and surface roughness. The O 1s intensity $I_{\mathrm{O\,1}s}$ falls to a steady-state nonzero value over a distance, 5–10 nm, that is consistent with the average peak-to-valley surface roughness (see below). $I_{\mathrm{O\,1}s}$ then remains constant for a film thickness $t = 45–50$ nm before falling to zero. This region of the sample contains the nanopipes whose internal surfaces adsorb oxygen upon air exposure. The remaining $\simeq 15$nm of ScN, prior to the rise of the Ti and the fall of the Sc 2p intensities, is fully dense with no nanopipes and thus exhibits no detectable oxygen signal. In contrast to these results, XPS depth profiles of samples that were capped *in situ* with 20-nm-thick *W* overlayers prior to air exposure showed that the entire ScN layers were oxygen free. This confirms that the oxygen detected in uncapped films enters the nanopipes from the free surface.

The surfaces of the ScN layers are rough and consist of mounds with, in the case of the 82-nm-thick ScN layer shown in the XTEM micrograph in Fig. 2(c), an average height of $\simeq 7$ nm. Similar mound structures have been observed previously in semiconductor,[19–23] metal,[24] and TM nitride[25,26] films grown at relatively low homologous temperatures. The primary origin of kinetic roughening is the

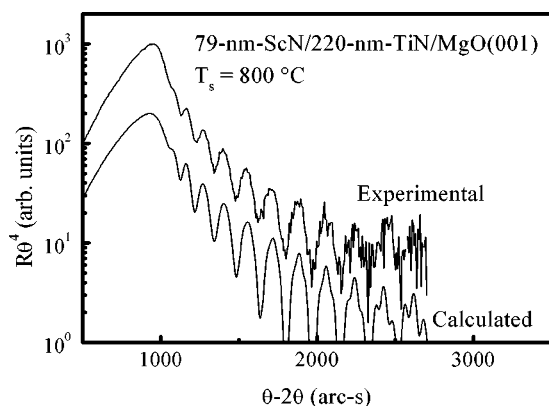

FIG. 4. Measured and simulated x-ray reflectivity scans from a 79-nm-thick epitaxial ScN layer on TiN/MgO(001).

presence of Ehrlich barriers[27] to the migration of adatoms over downsteps and/or deep traps at step edges on growing surfaces. This leads to a divergence in adatom flux and, hence, increased nucleation on terraces which in turn gives rise to surface roughening and faceting during film growth. In the plan-view image [Fig. 2(a)], the mounds appear as slightly darker regions while the valleys between them are somewhat brighter, due to thickness contrast. The valleys show a strong tendency to align along ⟨100⟩, directions with an average separation of $\simeq 40$ nm. From TEM observations of more than ten regions in each of five samples, the nanopipes themselves are bounded by {100} planes with little or no faceting. Thus, the nanopipes have rectangular cross sections with a typical size, as determined from plan-view TEM micrographs, of $\simeq 1.5 \times 5$ nm^2.

The mounds adjoin along low-energy ⟨100⟩, step edge directions (i.e., along Sc–N bonding directions) with the development of deep cusps. The local deposition rate at the bottom of the cusps is reduced due to atomic shadowing which, in combination with limited adatom mobility, gives rise to nanopipe development as discussed in Ref. 2. The observation that nanopipes form only above a critical film thickness ($t > t_c \simeq 15$ nm) indicates that surface roughening occurs gradually during growth and a critical mound height, which depends on both the angular incident flux distribution and the adatom mobility, is required to maintain continuously open nanopipe structures.

High-resolution x-ray reflectivity was used to obtain a quantitative measure of ScN film roughness over large lateral length scales. Figure 4 is a typical low-angle $\theta - 2\theta$ reflectivity scan from a 79-nm-thick ScN layer deposited on a 220-nm-thick TiN buffer layer on MgO(001). The reflectivity values are multiplied by θ^4 to account for the angular dependence of the intensity decrease from a perfectly flat surface.[28] Thus, the rate of decrease in measured $R\theta^4$ values with increasing θ is directly correlated to the surface roughness. The interference fringes in Fig. 4 arise from the presence of planar TiN/MgO and ScN/ TiN interfaces.

Measured x-ray reflectivity scans were fit to theoretical curves calculated from the recursive theory of Parrat based upon the Fresnel reflectivity formalism.[29] In this case, the sample is considered to consist of multiple layers, each having a constant electron density. The reflectivity of the top of each successive lamella is expressed in terms of its value at the top of the previous layer.[29] Roughnesses at the top surface and at each interface are modeled as Gaussian distributions of the interface position and are directly incorporated in the Fresnel coefficients. The measured and calculated curves in Fig. 4 are in very good agreement with respect to the angular position and intensity for all peaks, including the overall decay due to surface roughness.

From the results in Fig. 4, we obtain a root-mean-square (rms) surface roughness for the 79-nm-thick ScN film of 2.45 ± 0.10 nm. This corresponds to a peak-to-peak roughness amplitude of 6.9 nm, in excellent agreement with the value of 7 nm determined by XTEM [Fig. 2(c)]. The period of the oscillation indicates that the average thickness of the ScN layer is 78.8 ± 0.3 nm, very close to the thickness measured by XTEM for this layer, 82 nm. The modulation of the peak intensities in Fig. 4 becomes more apparent as θ increases due to a convolution of the ScN layer finite-thickness interference fringes with those of the TiN layer which is about three times thicker. The rms width of the ScN/TiN interface is only 0.5 ± 0.3 nm, consistent with the abrupt appearance in XTEM tilting experiments.

IV. CONCLUSIONS

Epitaxial stoichiometric ScN(001) films were grown on TiN(001) buffer layers on MgO(001) by ultrahigh-vacuum reactive magnetron sputter deposition in pure N_2 at $T_s = 800\,°C$. The films are in a mild state of in-plane compression due primarily to differential thermal contraction during sample cooling from T_s to room temperature. The relaxed ScN lattice constant, $a = 0.4501$ nm, and the Poisson ratio, $\nu = 0.20 \pm 0.04$, were determined by x-ray diffraction. ν_{ScN}, obtained from a combination of XRD reflection and transmission $\theta - 2\theta$ scans, is in excellent agreement with *ab initio* calculations.

The film growth temperature used in these experiments, $T_s = 800\,°C$, is relatively low with respect to the melting point of ScN.[30] Thus, low adatom mobilities during deposition result in kinetic surface roughening leading to the emergence of a periodic mound structure. After a critical thickness of $\simeq 15$ nm, deep cusps develop between mounds due to atomic shadowing which decreases the local deposition rate and leads to the formation of 1.5-nm-wide rectangular nanopipes extending along the growth direction. The nanopipes extend to the free surface and are self-organized along orthogonal ⟨100⟩ directions with an average separation of $\simeq 40$ nm. XTEM and x-ray reflectivity measurements show that the rms surface roughness of ScN layers with a thickness of 79 nm is 2.45 nm.

ACKNOWLEDGMENTS

This work was supported by the U.S. Department of Energy, Division of Materials Science, Grant No. DEFG02-96ER45439 through the University of Illinois Frederick Seitz Materials Research Laboratory. We also appreciate the use of the facilities of the MRL Center for Microanalysis of Materials, which is partially supported by DOE, at the Univer-

sity of Illinois. One of the authors (P.D.) is partially supported by the Fonds pour la Formation de Chercheurs et l'Aide à la Recherche (Québec, Canada).

[1] D. Gall, I. Petrov, L. D. Madsen, J.-E. Sundgren, and J. E. Greene, J. Vac. Sci. Technol. A **16**, 2411 (1998).
[2] D. Gall, I. Petrov, N. Hellgren, L. Hultman, J.-E. Sundgren, and J. E. Greene, J. Appl. Phys. **84**, 6034 (1998).
[3] R. C. Powell, N.-E. Lee, Y.-W. Kim, and J. E. Greene, J. Appl. Phys. **73**, 189 (1993).
[4] I. Petrov, F. Adibi, J. E. Greene, W. D. Sproul, and W.-D. Münz, J. Vac. Sci. Technol. A **10**, 3283 (1992).
[5] R. L. Doolittle, Nucl. Instrum. Methods Phys. Res. B **15**, 344 (1985).
[6] J. F. Moulder, W. F. Stichle, P. E. Sobol, and K. D. Bomben, *Handbook of X-Ray Photoelectron Spectroscopy,* edited by J. Chastain and R. C. King, Jr. (Physical Electronics, Eden Prairie, MN, 1995).
[7] Inorganic Index to Powder Diffraction File (Joint Committee on Powder Diffraction Standards, International Center for Powder Diffraction Data, Swarthmore, PA, 1997); MgO (Card No. 04-0820); TiN (Card No. 38-1420).
[8] H. Ljungcrantz, M. Odén, L. Hultman, J. E. Greene, and J.-E. Sundgren, J. Appl. Phys. **80**, 6725 (1996).
[9] B. Hajek, V. Brozek, and H. Duvigneaud, J. Less-Common Met. **33**, 385 (1973).
[10] K. Aigner, W. Lengauer, D. Rafaja, and P. Ettmayer, J. Alloys Compd. **215**, 121 (1994).
[11] H. Landolt and R. Börnstein, *Numerical Data and Functional Relationships in Science and Technology, Group III* (Springer, Berlin, 1975), Vol. 7, Pt. b1, p. 27.
[12] J. A. Sue, Surf. Coat. Technol. **54/55**, 154 (1992).
[13] W. Lengauer, Solid State Chem. **76**, 412 (1988).
[14] W. Lengauer, P. Ettmayer, and K. Yvon, J. Less-Common Met. **168**, L7 (1991).
[15] J. C. Schuster and J. Bauer, J. Less-Common Met. **109**, 345 (1985).
[16] E. Török, A. J. Perry, L. Chollot, and W. D. Sproul, Thin Solid Films **153**, 37 (1987).
[17] J. O. Kim, J. D. Achenbach, P. B. Mirkarimi, M. Shinn, and S. A. Barnett, J. Appl. Phys. **72**, 1805 (1992).
[18] R. M. Dreizler and E. K. U. Gross, *Density Functional Theory* (Springer, Berlin, 1990).
[19] N.-E. Lee, D. G. Cahill, and J. E. Greene, J. Appl. Phys. **80**, 2199 (1996).
[20] G. Xue, H. Z. Xiao, M.-A. Hasan, J. E. Greene, and H. K. Birnbaum, J. Appl. Phys. **74**, 2512 (1993).
[21] N.-E. Lee, G. A. Tomasch, and J. E. Greene, Appl. Phys. Lett. **65**, 3236 (1994).
[22] N.-E. Lee, G. Xue, and J. E. Greene, J. Appl. Phys. **80**, 2199 (1996).
[23] D. J. Eaglesham, H.-J. Gossmann, and M. Cerullo, Phys. Rev. Lett. **65**, 1227 (1990).
[24] J. A. Stroscio, D. T. Pierce, M. D. Stiles, A. Zangwill, and L. M. Sander, Phys. Rev. Lett. **75**, 4246 (1995).
[25] B. W. Karr, I. Petrov, D. G. Cahill, and J. E. Greene, Appl. Phys. Lett. **70**, 1703 (1997).
[26] B. W. Karr, I. Petrov, P. Desjardins, D. G. Cahill, and J. E. Greene, Surf. Coat. Technol. **94/95**, 403 (1997).
[27] S. C. Wang and G. Ehrlich, Phys. Rev. Lett. **70**, 41 (1993); **71**, 4174 (1993); G. Ehrlich, Surf. Sci. **331/333**, 865 (1995); A. Gölzhäuser and G. Ehrlich, Phys. Rev. Lett. **77**, 1334 (1996).
[28] E. Chason and T. M. Mayer, Crit. Rev. Solid State Mater. Sci. **22**, 1 (1997).
[29] L. G. Parrat, Phys. Rev. **95**, 395 (1954).
[30] The ScN melting point is unknown. However, based upon XRD measurements it is $>1500\,°C$ (Ref. 14).